Use of the floating frame of reference formulation in large deformation analysis: Experimental and numerical validation

4 authors, including:

Some of the authors of this publication are also working on these related projects:

Vibration Absorbers View project

"Remotely Operated Robots with Application to Landmines Removal in Egypt", STDF Grant # 465 View project

Use of the floating frame of reference formulation in large deformation analysis: experimental and numerical validation

A A Nada[1]**, B A Hussein**[2]**, S M Megahed**[3*]**,** and **A A Shabana**[2]
[1]Benha Institute of Technology, Benha University, Qalubia, Egypt
[2]University of Illinois at Chicago, Chicago, Illinois, USA
[3]Mechanical Design and Production Engineering Department, Faculty of Engineering, Cairo University, Giza, Egypt

Abstract: The finite-element *floating frame of reference* (FFR) formulation is used, for the most part, in the small deformation analysis of flexible bodies that undergo large reference displacements. This formulation allows for filtering out systematically complex shapes associated with high frequencies that have no significant effect on the solution in the case of small deformations. The resulting low-order FFR models have been widely used to obtain efficient and accurate solutions for many engineering and physics applications. In this investigation, the use of the FFR formulation in the large deformation analysis is examined, and it is demonstrated that large deformation FFR models can be accurate in applications, where the deformation can be described using simple shapes as it is the case in robot system manipulators. In these cases, the standard finite-element FFR formulation must be used with non-linear strain–displacement relationships that account for the geometric non-linearities. The results obtained using the large deformation FFR models are compared with the results obtained using the large deformation *absolute nodal coordinate formulation* (ANCF), which does not allow for the use of linear modes. The ANCF models are developed using two different methods for formulating the elastic forces: the basic *continuum mechanics approach* (ANCF-BC) and the *elastic line method* (ANCF-EL). While the explicit Adams method can be used to obtain the numerical solution of the FFR model, two implicit integration methods are implemented in order to be able to obtain an efficient solution of the FFR and ANCF models. These implicit integration methods are the RADAU5 method and the *Hilber–Hughes–Taylor* (HHT) method. In the case of simple large deformation shapes, the simulation results obtained in this study show a good agreement between the FFR and the ANCF solutions. The results also show that, in the case of thin and stiff beams, the coupled deformation modes that result from the use of the ANCF-BC can be a source of numerical and locking problems, as reported in the literature. These ANCF-BC numerical problems can be circumvented using the implicit HHT integration method. Nonetheless, the HHT integrator does not capture high-frequency FFR axial modes which are necessary in order to obtain accurate solutions for high-speed rotating beams. In addition to the comparison with the ANCF solutions, experimental results of a forward dynamics model are used in this study to validate the large deformation FFR numerical solutions. The experimental set-up used in the validation of the numerical solutions is also described in this investigation.

Keywords: floating frame of reference, absolute nodal coordinate formulation, flexible manipulators, coupled deformation modes

Corresponding author: Mechanical Design and Production Engineering Department, Faculty of Engineering, Cairo University, 1 AlGamea St., Giza 12613, Egypt.
email: smegahed@cu.edu.eg; smegahed@yahoo.com

1 INTRODUCTION

For the most part, the finite-element *floating frame of reference* (FFR) formulation has been used in the small deformation analysis of flexible multibody system applications. In this formulation, which allows for systematically filtering out complex shapes associated with high frequencies that have no significant effect on the solution, two sets of coordinates are used. The first set has the reference coordinates that define the location and orientation of the body coordinate system, whereas the second set has the elastic coordinates that describe the deformation with respect to the body coordinate system. Using these coordinate sets, a local linear problem can be defined, allowing for the use of modal reduction techniques [1, 2]. The resulting reduced-order model includes only low-frequency modes that assume simple shapes and can be significant in the analysis of small deformations [3]. In the case of small deformations, linear strain–displacement relationships can be used, leading to a constant stiffness matrix. The FFR mass matrix, on the other hand, is highly non-linear because of the geometric non-linearities resulting from the finite rotation of the body reference. Efficient numerical solution of small deformation multibody system problems based on the FFR formulation can be obtained using well-developed numerical integration methods and sparse matrix techniques [4].

The FFR formulation has been used in a small number of investigations in the large deformation analysis of flexible multibody systems. Most of these investigations employ a sub-structuring method in which each finite element is treated as a separate flexible body and is assigned its FFR. These finite elements are connected by non-linear rigid joints in order to obtain the equations of the flexible body. The use of this approach has several computational drawbacks including large dimensionality and the difficulty in employing modal reduction techniques that allow for filtering out high-frequency modes. It is demonstrated in this investigation that the finite-element FFR formulation can effectively be used in the large deformation analysis without the need for assigning each element its FFR, thereby allowing for assembling the finite elements of a flexible body using the standard finite-element assembly procedure. It is important, however, to point out that the FFR formulation as presented in this investigation can only be used in the analysis of the large deformation when such a deformation can be described using simple shapes. Furthermore, non-linear strain–displacement relationships must be used in order to capture the effect of the geometric non-linearities due to the large deformation. Therefore, both the mass and stiffness matrices in the large deformation FFR formulation used in this investigation are non-linear functions of the body coordinates. This non-linear

FFR formulation, however, allows for systematically eliminating high-frequency modes because simple deformation shapes are assumed, and consequently, modal reduction techniques can be applied.

The large deformation FFR solution can be validated numerically using other large deformation formulations such as the *absolute nodal coordinate formulation* (ANCF) [2, 5–8]. The FFR formulation and the ANCF employ conceptually different methods for the motion description. While both formulations can describe correctly arbitrary rigid body displacements [2], ANCF does not use a local frame of reference to formulate the inertia forces. Unlike the FFR formulation, ANCF leads to a constant mass matrix and zero Coriolis and centrifugal forces. On the other hand, ANCF leads to a more complex expression for the elastic forces and does not allow for the use of linear modes because the deformation and the reference motion are not separated. The large deformation FFR solution obtained using modal reduction techniques will be compared with the ANCF solution obtained using the nodal coordinates instead of modal coordinates used with the FFR formulation.

In rotating and spinning structure applications, it is necessary to include the effect of the axial modes in order to be able to obtain an accurate solution. Axial modes can be much stiffer than transverse deformation modes, and as a consequence, the use of explicit integration methods in such cases can be inefficient as compared to the use of implicit integration methods. As shown in this study, some implicit integration methods can fail to capture the effect of high-frequency axial modes, and therefore, the solution obtained using these implicit integration methods must be carefully examined. Explicit integration methods, on the other hand, can be used to obtain an efficient numerical solution of the FFR model when high-frequency axial modes are eliminated [9]. If axial modes are considered, the effect of these modes appears in many applications as high-frequency oscillations superimposed on a nominal solution dominated by the transverse vibration modes. These high-frequency oscillations introduce geometric stiffness that can have a significant effect on the solution in the neighbourhood of critical speeds [10, 11]. Implicit integration methods that require the use of the iterative Newton–Raphson algorithm may filter out the effect of the axial modes by eliminating the associated high-frequency oscillations. In order to examine the use of implicit integration methods in solving this type of problems, the two implicit integration methods RADAU5 and the *Hilber–Hughes–Taylor* (HHT) methods are implemented. As reported in the literature, implicit integration methods can be used to obtain an efficient solution for the ANCF models, which do not use linear modes [12, 13]. Such more detailed models include the effects of coupled deformation modes [6, 12, 14], and therefore these ANCF

models do not suffer from the same problems as the FFR models that are based on linear modes. Nonetheless, in the case of simple large deformation shapes, a good agreement between the FFR and the ANCF solutions can be obtained as demonstrated in this study. In order to numerically validate the large deformation FFR solutions, the ANCF models can be developed using two different methods for formulating the elastic forces: the basic *continuum mechanics approach* (ANCF-BC) and the *elastic line method* (ANCF-EL). As reported in the literature, in the case of thin and stiff beams, the coupled deformation modes that result from the use of the ANCF-BC can be a source of numerical and locking problems. These ANCF-BC numerical problems can be circumvented using the implicit HHT integration method. Nonetheless, as previously mentioned, the HHT integrator may fail to capture high-frequency FFR axial modes that are necessary in order to obtain accurate solutions for high-speed rotating beams.

In addition to the comparison with the ANCF solutions, experimental results of a forward dynamics model are used in this study to validate the large deformation FFR numerical solutions. To this end, a simple robot arm is used in the experimental study presented in this article [1]. The rate of change of the manipulator rotation makes the effect of centrifugal stiffening terms more significant. While for most flexible robotic manipulators, the link axial and torsional vibration modes can be neglected, in solving rotating beam problems using the FFR formulation, an incorrect and unstable solution is obtained if the axial modes are neglected due to lack of the geometric stiffening effect, as previously mentioned [10, 11]. In this study, the large transverse deformation of the robot arm is measured, and the measured experimental results are compared with the numerical results obtained using the FFR and ANCF models. The experimental set-up used in the validation of the numerical solutions, which is described in this investigation, uses a thin beam to represent the flexible robot arm. The FFR model that will be used in this study to obtain the numerical results that will be compared with the experimental results is the conventional three-dimensional (3D) beam element that employs infinitesimal rotations as nodal coordinates. While different types of ANCF elements can be used in the finite-element formulation of large deformation problems of flexible manipulators, the 3D fully parameterized beam element [15, 16] is used to obtain the large deformation ANCF results that will be compared with the FFR and experimental results.

This investigation makes three new contributions that can be summarized as follows:

(a) numerical validation of the 3D large deformation finite-element FFR formulation by comparison with the results obtained using the large deformation ANCF models;

(b) implementation of the implicit numerical integration methods in the large deformation FFR algorithm in order to examine whether or not such integration methods are capable of capturing the effect of the relatively stiff axial modes;

(c) experimental validation of the 3D large deformation finite-element FFR formulation by comparing the numerical and experimental results.

2 LARGE DEFORMATION FFR FORMULATION

In the FFR formulation, the deformation shape is defined in the selected body coordinate system. Such a description has a clear advantage in the case of small deformation problems since a local linear problem can be defined, thereby allowing for systematically applying modal synthesis techniques that can lead to a significantly lower-dimensional model. While, in general, there is no clear advantage in using the FFR formulation in the large deformation analysis, there are important applications such as flexible robot arms, helicopter rotors, flexible space structures, and many others, in which the large deformation can be represented using simple shapes that can be defined in the body coordinate systems. In these cases, the use of the finite-element FFR formulation can lead to a much more efficient solution as compared to other large deformation finite-element formulations. There are, however, several fundamental issues related to the numerical and experimental validation of the results and the accuracy of the numerical solution when relatively stiff modes are considered with explicit and implicit numerical integration methods. These fundamental issues will be considered in later sections of this article. In this section, the kinematic description used in the FFR formulation is briefly reviewed.

In the FFR formulation, the global position vector of an arbitrary point P on a flexible body can be written as

$$\mathbf{r} = \mathbf{R} + \mathbf{A}\bar{\mathbf{u}} \qquad (1)$$

where the vector $\mathbf{R}$ defines the location of the origin of the body coordinate system xyz, $\mathbf{A} = \mathbf{A}(\boldsymbol{\theta})$ is the transformation matrix that defines the orientation of the local coordinate system xyz with respect to the inertial frame XYZ as function of the selected orientation parameters $\boldsymbol{\theta}$, and $\bar{\mathbf{u}}$ is the vector that defines the location of the arbitrary point with respect to the body coordinate system. In this investigation, the four Euler parameters are used in order to avoid the singularity problem associated with the three-parameter representation [2].

The position vector $\bar{\mathbf{u}}$ of point P, which is defined in the local coordinate system xyz, can be expressed in
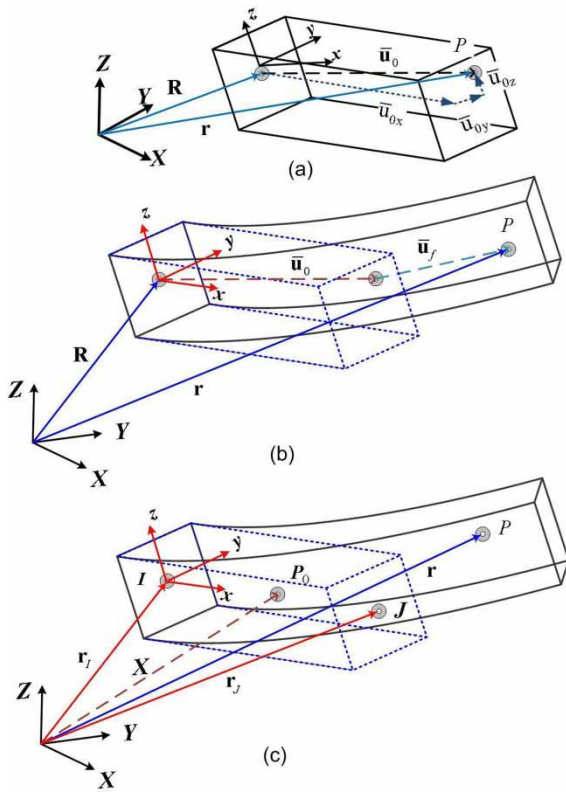
Fig. 1 Coordinate system: (a) rigid body case, (b) FFR formulation, and (c) ANCF

terms of the elastic coordinates as follows

$$\bar{\mathbf{u}} = \bar{\mathbf{u}}_0 + \bar{\mathbf{u}}_f = \bar{\mathbf{u}}_0 + \mathbf{S}\mathbf{q}_f \qquad (2)$$

where $\bar{\mathbf{u}}_0 = \begin{bmatrix} \bar{u}_{x0} & \bar{u}_{y0} & \bar{u}_{z0} \end{bmatrix}^T$ is the position vector of point P in the undeformed state (see Figs 1(a) and (b)), $\mathbf{S}$ is the shape function matrix, and $\mathbf{q}_f$ is the vector of the generalized elastic coordinates, defined in the local coordinate system xyz. A kinematic equation similar to the preceding equation can be defined for each finite element of a flexible body. These finite elements by introducing the concept of the *finite-element intermediate coordinate system* can be assembled using a standard finite-element assembly procedure. The 3D beam element shape function matrix used in this investigation with the FFR formulation is presented in Appendix 1 of this article.

Using the kinematic description of the finite-element FFR formulation, the vector of coordinates of a flexible body in the multibody system can be expressed in the following partitioned form

$$\mathbf{q}_{rf}^i = \begin{bmatrix} \mathbf{q}_r^T & \mathbf{q}_f^T \end{bmatrix}^T = \begin{bmatrix} \mathbf{R}^T & \boldsymbol{\theta}^T & \mathbf{q}_f^T \end{bmatrix}^T \qquad (3)$$

The FFR formulation leads to exact modelling of the rigid body dynamics when the structures rotate as rigid bodies. In the case of a rigid body displacement, the elastic coordinates $\mathbf{q}_f$ are equal to zero, leading to zero strains in the case of a rigid body motion.

If the shape of the large deformation is assumed to be simple, the vector of elastic nodal coordinates $\mathbf{q}_f$ can be expressed in terms of the modal coordinates, leading to a lower-dimensional model that includes only significant deformation modes.

3 FFR LARGE DEFORMATION GEOMETRIC NON-LINEARITIES

In the case of the large deformation analysis, non-linear strain–displacement relationships must be used in order to capture the effect of geometric non-linearities. The vector of the elastic forces $\mathbf{Q}_k$ can be obtained by differentiating the strain energy U with respect to the elastic coordinate vector $\mathbf{q}_f$ as $\mathbf{Q}_k = -(\partial U/\partial \mathbf{q}_f)^T$, where the strain energy U can be written as

$$U = \frac{1}{2} \int_V \boldsymbol{\varepsilon}^T \boldsymbol{\sigma} \, dV = \frac{1}{2} \int_V \boldsymbol{\varepsilon}^T \mathbf{E} \boldsymbol{\varepsilon} \, dV \qquad (4)$$

In this equation, V is the volume, $\mathbf{E}$ is the matrix of the material elastic coefficients, $\boldsymbol{\varepsilon}$ is the strain vector, and $\boldsymbol{\sigma}$ is the stress vector. The displacement of an arbitrary point on the beam is related to the deformation along its neutral axis by the following equation (see Fig. 2)

$$\bar{\mathbf{u}}_f = \begin{bmatrix} u \\ v \\ w \end{bmatrix} = \begin{bmatrix} u_0 - y\dfrac{\partial v_0}{\partial x} - z\dfrac{\partial w_0}{\partial x} \\ v_0 - z\varphi_0 \\ w_0 + y\varphi_0 \end{bmatrix} \qquad (5)$$

where $\bar{\mathbf{u}}_f = \begin{bmatrix} u & v & w \end{bmatrix}^T$ is the vector of elastic displacements, subscript 0 refers to the centroidal axis, φ_0 is the twist angle, (x, y, z) are the coordinates of the material point in the beam undeformed configuration with respect to the body coordinate system. The preceding equation defines, respectively, the in- and out-of-plane transverse displacements u and w assuming small rotations due to bending and twist angle φ_0, i.e. the displacement field is linearized with respect to rotations due to deformation. The shear deformation resulting from the shear force at the cross-section of the beam is considered in this study. For the two-node
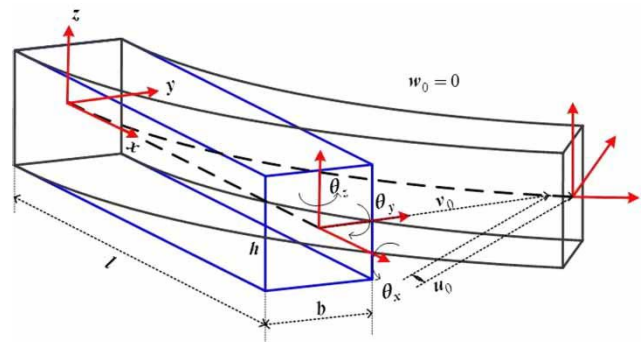

Fig. 2 Beam element displacement field

beam finite element used in this investigation, the 12×1 vector of element nodal coordinates $\mathbf{q}_f$ is given by

$$\mathbf{q}_f = \begin{bmatrix} u_I & v_I & w_I & \theta_{xI} & \theta_{yI} & \theta_{zI} & u_J & v_J & w_J & \theta_{xJ} & \theta_{yJ} & \theta_{zJ} \end{bmatrix}^T \quad (6)$$

The strain energy of the beam element can be formulated to include the contributions from the axial strain ε_{xx} and shearing strains ε_{xy} and ε_{xz}, while the effects of other strain components are neglected by using the appropriate form of the matrix of elastic coefficients $\mathbf{E}$ as discussed by Nada [1]. Therefore the strain energy of equation (4) may be written as

$$U = \frac{1}{2} \int_V \left[E\varepsilon_{xx}^2 + 4G(\varepsilon_{xy}^2 + \varepsilon_{xz}^2) \right] dV = U_A + U_S \quad (7)$$

where E is the modulus of elasticity, and G is the modulus of rigidity. The first energy term U_A represents the contribution due to the axial strain, while the second energy term U_S is due to the shearing strains. By neglecting higher-order terms and those involving fourth moments of area in the axial strain energy, and retaining only the linear contribution in U_S, the simplified expression of U in the case of a flexible rotating arm can be written as [1]

$$U = U_{A,L} + U_{S,L} + U_G + U_B \quad (8)$$

where

$$U_{A,L} = \frac{EA}{2} \int_l \left(\frac{\partial u_0}{\partial x} \right)^2 dx + \frac{EI_{zz}}{2} \int_l \left(\frac{\partial^2 v_0}{\partial x^2} \right)^2 dx$$
$$+ \frac{EI_{yy}}{2} \int_l \left(\frac{\partial^2 w_0}{\partial x^2} \right)^2 dx$$

$$U_{S,L} = \frac{GI_{xx}}{2} \int_l \left(\frac{\partial \varphi_0}{\partial x} \right)^2 dx$$

$$U_G = \frac{EA}{2} \int_l \left[\left(\frac{\partial u_0}{\partial x} \right) \left(\frac{\partial v_0}{\partial x} \right)^2 + \left(\frac{\partial u_0}{\partial x} \right) \left(\frac{\partial w_0}{\partial x} \right)^2 \right] dx$$

$$U_B = \frac{EA}{8} \int_l \left[\left(\frac{\partial v_0}{\partial x} \right)^4 + \left(\frac{\partial w_0}{\partial x} \right)^4 + 2 \left(\frac{\partial v_0}{\partial x} \right)^2 \right.$$
$$\left. \times \left(\frac{\partial w_0}{\partial x} \right)^2 \right] dx \quad (9)$$

where $U_{A,L}$, $U_{S,L}$, U_G, and U_B are the axial, shear, geometric, and bending terms.

3.1 Constant stiffness matrix $\mathbf{K}_{ff,L}$

The linear part of the strain–displacement relations leads to the following part of the strain energy

$$U_L = (U_{A,L} + U_{S,L})$$
$$= \frac{EA}{2} \int_l \left(\frac{\partial u_0}{\partial x} \right)^2 dx + \frac{EI_{zz}}{2} \int_l \left(\frac{\partial^2 v_0}{\partial x^2} \right)^2 dx$$

$$+ \frac{EI_{yy}}{2} \int_l \left(\frac{\partial^2 w_0}{\partial x^2} \right)^2 dx + \frac{GI_{xx}}{2} \int_l \left(\frac{\partial \varphi_0}{\partial x} \right)^2 dx \quad (10)$$

The elastic forces in this special case can be obtained by using the equation $\mathbf{Q}_k = -(\partial U_L / \partial \mathbf{q}_f)^T = -\mathbf{K}_{ff,L} \mathbf{q}_f$. In this equation, $\mathbf{K}_{ff,L}$ is the constant stiffness matrix of the 3D straight element of uniform cross-section. The matrix $\mathbf{K}_{ff,L}$, which is the same as the conventional stiffness matrix used in linear structural dynamics, does not contain coupling between the axial and bending deformation of the finite element. Therefore, this matrix does not capture the effect of the geometric stiffness and its use alone does not lead to a correct solution at critical speeds. The stiffness matrix $\mathbf{K}_{ff,L}$ is used in this investigation with the constant mass matrix associated with the elastic coordinates to obtain the system eigen vectors that are used to define the shapes of the large deformation with respect to the body coordinate system.

3.2 Geometric stiffness matrix $\mathbf{K}_{ff,G}$

The geometric stiffness matrix has terms that couple the axial and transverse displacements, and therefore, accounts for the geometric stiffening. This geometric stiffness matrix can be defined by using the part U_G of the strain energy as $(\partial U_G / \partial \mathbf{q}_f)^T = \mathbf{K}_{ff,G}(\mathbf{q}_f) \mathbf{q}_f$, where the geometric stiffness matrix $\mathbf{K}_{ff,G}$ for the 3D beam element presented in Appendix is defined as

$$\mathbf{K}_{ff,G} = \frac{EA(u_1 - u_2)}{\ell^2}$$

$$\times \begin{bmatrix}
0 & 0 & 0 & 0 & 0 & 0 \\
0 & 6/5 & 0 & 0 & 0 & \ell/10 \\
0 & 0 & 6/5 & 0 & -\ell/10 & 0 \\
0 & 0 & 0 & \gamma & 0 & 0 \\
0 & 0 & -1/10\ell & 0 & 2\ell^2/15 & 0 \\
0 & \ell/10 & 0 & 0 & 0 & 2\ell^2/15 \\
0 & 0 & 0 & 0 & 0 & 0 \\
0 & -6/5 & 0 & 0 & 0 & -\ell/10 \\
0 & 0 & -6/5 & 0 & \ell/10 & 0 \\
0 & 0 & 0 & -\gamma & 0 & 0 \\
0 & 0 & -\ell/10 & 0 & 0 & -1/30\ell^2 \\
0 & \ell/10 & 0 & 0 & 0 & -\ell^2/30 \\
\end{bmatrix}$$

$$\begin{bmatrix}
0 & 0 & 0 & 0 & 0 & 0 \\
0 & -6/5 & 0 & 0 & 0 & \ell/10 \\
0 & 0 & -6/5 & 0 & -\ell/10 & 0 \\
0 & 0 & 0 & -\gamma & 0 & 0 \\
0 & 0 & 1/10 & 0 & 0 & 0 \\
0 & -\ell/10 & 0 & 0 & -\ell^2/30 & -\ell^2/30 \\
0 & 0 & 0 & 0 & 0 & 0 \\
0 & 0 & 0 & 0 & 0 & -\ell/10 \\
0 & 0 & 6/5 & 0 & 1/10\ell & 0 \\
0 & 6/5 & 0 & \gamma & 0 & 0 \\
0 & 0 & \ell/10 & 0 & 2\ell^2/15 & 0 \\
0 & -\ell/10 & 0 & 0 & 0 & 2\ell^2/15 \\
\end{bmatrix} \quad (11)$$

Using this matrix, the non-linear elastic forces of the flexible body can be updated to include the effect of the geometric stiffness matrix as

$$\mathbf{Q}_k = \left[\mathbf{K}_{ff,L}(\mathbf{q}_f) + \mathbf{K}_{ff,G}(\mathbf{q}_f) \right] \mathbf{q}_f \tag{12}$$

The generalized modal forces associated with the modal coordinates of the flexible body can be obtained from the vector $\mathbf{Q}_k$ by using the modal transformation. The non-linear elastic force vector of equation (12) accounts for the coupling between the axial and transverse deformations. It is known that implicit integration methods lead to efficient solution and smooth results for stiff systems because such integration methods can filter out high frequencies. It is, therefore, important to examine the effect of using these implicit integration methods with the large deformation FFR formulation that allows for inclusion or exclusion of vibration modes.

3.3 Centrifugal and Coriolis forces

The finite rotation of the body reference in the FFR formulation also introduces geometric non-linearities that result in a highly non-linear mass matrix. As a consequence, the centrifugal and Coriolis forces are not equal to zero and they must be included in the FFR equations of motion. Using the definition of the kinetic energy and the mass matrix, the quadratic velocity centrifugal and Coriolis force vector $\mathbf{Q}_v$ can be obtained in a closed form as follows

$$\mathbf{Q}_v = \begin{bmatrix} \mathbf{Q}_{vR}^T & \mathbf{Q}_{v\theta}^T & \mathbf{Q}_{vf}^T \end{bmatrix}^T = \left(\frac{\partial T}{\partial \mathbf{q}} \right)^T - \dot{\mathbf{M}}\dot{\mathbf{q}} \tag{13}$$

A more explicit form of the components $\mathbf{Q}_{vR}$, $\mathbf{Q}_{v\theta}$, and $\mathbf{Q}_{vf}$ is given as

$$\mathbf{Q}_{vR} = -\mathbf{A} \left(\tilde{\bar{\omega}}^2 \bar{\mathbf{L}} + 2\tilde{\bar{\omega}} \bar{\mathfrak{S}}^{(2)} \dot{\mathbf{q}}_f \right)$$
$$\mathbf{Q}_{v\theta} = -2\dot{\bar{\mathbf{G}}}^T \bar{\mathbf{I}}_{\theta\theta} \bar{\omega} - 2\dot{\bar{\mathbf{G}}}^T \bar{\mathbf{I}}_{\theta f} \dot{\mathbf{q}}_f - \bar{\mathbf{G}}^T \dot{\bar{\mathbf{I}}}_{\theta\theta} \bar{\omega}$$
$$\mathbf{Q}_{vf} = -\int_V \rho \mathbf{S}^T \left(\tilde{\bar{\omega}}^2 \bar{\mathbf{u}} + 2\tilde{\bar{\omega}} \dot{\bar{\mathbf{u}}}_f \right) dV \tag{14}$$

In this equation, ρ and V are the mass density and volume, $\mathbf{A}$ is the transformation matrix that defines the orientation of the FFR, $\bar{\omega}$ is the FFR angular velocity defined in the body coordinate system, $\tilde{\bar{\omega}}$ is the skew symmetric matrix associated with the vector $\bar{\omega}$, $\bar{\mathbf{G}}$ is the matrix that relates the time derivatives of the orientation parameters to the angular velocity vector $\bar{\omega}$, $\bar{\mathbf{I}}_{\theta\theta}$ is the inertia tensor of the flexible body defined in the body coordinate system, and $\tilde{\bar{\mathbf{L}}}$ is the skew symmetric matrix associated with the vector $\bar{\mathbf{L}}$, which can be written in terms of two inertia shape integrals as $\bar{\mathbf{L}} = \bar{\mathfrak{S}}^{(1)} + \bar{\mathfrak{S}}^{(2)} \mathbf{q}_f$, where $\bar{\mathfrak{S}}^{(1)} = \int_V \rho \bar{\mathbf{u}}_0 \, dV$ and $\bar{\mathfrak{S}}^{(2)} = \int_V \rho \mathbf{S} \, dV$.

4 THREE-DIMENSIONAL NUMERICAL VALIDATION OF FFR FORMULATION

One of the main contributions of this investigation is the experimental and 3D numerical validation of the large deformation FFR formulation discussed in the preceding section. For the numerical validation, the conceptually different large deformation ANCF that leads to significantly different structure of the equations of motion is used. Unlike the large deformation FFR discussed in the preceding section, ANCF finite elements lead to a constant mass matrix and zero centrifugal and Coriolis forces. ANCF finite elements capture coupled deformation modes and account for the geometric stiffness in different ways. Figure 1(c) shows the coordinates used to define the ANCF absolute position and gradient coordinates of the fully parameterized beam element used in this numerical validation. The global position vector $\mathbf{r}$ of the material point P on the beam element can be defined by using the element shape function as

$$\mathbf{r} = \mathbf{Se} \tag{15}$$

where $\mathbf{S}$ is the element shape function matrix, and $\mathbf{e}$ is the vector of element nodal coordinates, which does not contain infinitesimal or finite rotation coordinates. In the preceding equation, the beam is considered as a continuous volume, making it possible to relax the assumption of the rigidity of the cross-sections. Therefore, in large deformation problems the cross-section may deform and change its orientation with respect to the centre-line. For a fully parameterized 3D beam element (see Fig. 1(c)), 12 nodal coordinates are used for each node. The coordinates of node I is denoted as $\mathbf{e}_I$ and can be written in the following form

$$\mathbf{e}_I = \begin{bmatrix} \mathbf{r}_I^T & \dfrac{\partial \mathbf{r}_I}{\partial x}^T & \dfrac{\partial \mathbf{r}_I}{\partial y}^T & \dfrac{\partial \mathbf{r}_I}{\partial z}^T \end{bmatrix}^T \tag{16}$$

where the vector $\mathbf{r}_I$ defines the global position of node I and the three vectors $\partial \mathbf{r}_I / \partial x$, $\partial \mathbf{r}_I / \partial y$, and $\partial \mathbf{r}_I / \partial z$ define the position vector gradients (slopes) at node I. The nodal coordinates of the element can then be given by the vector $\mathbf{e} = \begin{bmatrix} \mathbf{e}_I^T & \mathbf{e}_J^T \end{bmatrix}^T = \mathbf{q}_e$. Using the ANCF motion description, one can show that the element mass matrix is always constant, and as a consequence, the vector of centrifugal and Coriolis forces is identically equal to zero. On the other hand, ANCF allows the use of different methods for formulating the elastic forces. In this investigation, the continuum mechanics and the elastic line approaches are used. In both cases, one can formulate the strain energy expression U_e and obtain the elastic forces using the equation $\mathbf{Q}_k = -(\partial U_e / \partial \mathbf{e})^T = -\mathbf{K}(\mathbf{e})\mathbf{e}$, where $\mathbf{K}$ is the stiffness matrix that is highly non-linear function of the absolute coordinates.

4.1 Continuum mechanics approach (ANCF-BC)

The general continuum mechanics approach can be used to define the non-linear elastic forces of fully parameterized ANCF beam or plate elements. The non-linear Green–Lagrange strain tensor is calculated from the matrix of *position vector gradients* $\mathbf{D}$, which can be written as follows [17]

$$\mathbf{D} = \frac{\partial \mathbf{r}}{\partial \mathbf{X}} = \frac{\partial \mathbf{r}}{\partial \mathbf{x}} \frac{\partial \mathbf{x}}{\partial \mathbf{X}} = \mathbf{J}\mathbf{J}_0^{-1} \tag{17}$$

where $\mathbf{X}$ is the vector of coordinates of an arbitrary material point P_0 in the undeformed reference configuration as shown in Fig. 1(c), $\mathbf{x}$ is the vector of the local spatial element coordinates in the reference configuration, $\mathbf{J} = \partial \mathbf{r}/\partial \mathbf{x}$, and $\mathbf{J}_0 = \partial \mathbf{X}/\partial \mathbf{x}$. Note that the matrix $\mathbf{J}_0$ is constant. The Lagrangian strain tensor $\boldsymbol{\varepsilon}$ can be defined as $\boldsymbol{\varepsilon} = (\mathbf{D}^T \mathbf{D} - \mathbf{I})/2$. Using this definition of the strain tensor and the constitutive equations, the strain energy can be defined and used to derive the expressions for the generalized forces. The use of the ANCF-BC approach for formulating the elastic forces leads to a model that includes coupled deformation modes and accounts for all geometric non-linearities.

4.2 Elastic line approach (ANCF-EL)

An alternative method that can be used for formulating the ANCF elastic forces is the elastic line approach [6]. In this approach, the extension, shear, torsion, and bending are defined at the element elastic line. The curvature expression is used to define the bending strains. The vectors of position gradients along the beam centre-line are defined as follows

$$\mathbf{r}_{0x} = \mathbf{r}_{,x}(x, 0, 0), \quad \mathbf{r}_y = \mathbf{r}_{,y}(x, 0, 0), \quad \mathbf{r}_z = \mathbf{r}_{,z}(x, 0, 0) \tag{18}$$

where the vector $\mathbf{r}_{0x}$ is tangent to the beam centre-line, and the vectors $\mathbf{r}_y$ and $\mathbf{r}_z$ define the shear plane at an arbitrary point x on the beam centre-line. The strain components along the beam centre-line can be defined using the Lagrange strain tensor and the curvature for the element as

$$\varepsilon_{xx} = \frac{1}{2}\left(\mathbf{r}_{0x}^T\mathbf{r}_{0x} - 1\right), \quad \varepsilon_{yy} = \frac{1}{2}\left(\mathbf{r}_y^T\mathbf{r}_y - 1\right)$$

$$\varepsilon_{zz} = \frac{1}{2}\left(\mathbf{r}_z^T\mathbf{r}_z - 1\right)$$

$$\gamma_{xy} = \mathbf{r}_{0x}^T\mathbf{r}_y, \quad \gamma_{xz} = \mathbf{r}_{0x}^T\mathbf{r}_z, \quad \gamma_{yz} = \mathbf{r}_y^T\mathbf{r}_z$$

$$\kappa_x = \frac{1}{2}\left(\mathbf{r}_z^T\mathbf{r}_{0xy} - \mathbf{r}_y^T\mathbf{r}_{0xz}\right), \quad \kappa_y = \mathbf{r}_z^T\mathbf{r}_{0xx}$$

$$\kappa_z = -\mathbf{r}_y^T\mathbf{r}_{0xx} \tag{19}$$

where $\mathbf{r}_{0xx} = \partial^2\mathbf{r}(x, 0, 0)/\partial x^2$, $\mathbf{r}_{0xy} = \partial^2\mathbf{r}(x, 0, 0)/\partial x\partial y$, and $\mathbf{r}_{0xz} = \partial^2\mathbf{r}(x, 0, 0)/\partial x\partial z$. Using the preceding

equation, the total strain energy of the beam can be written as the sum of extension, shear, and bending strain energies defined as $U = U_A + U_S + U_T + U_B$. The forms of the strain energies are presented by Schwab and Meijaard [6]. As reported in the literature, because of the kinematic definitions presented in this section, the ANCF-EL approach leads to more efficient solution for the equation of motion because such an approach leads to models that do not include coupled deformation modes that can be the source of locking problems when fully parameterized ANCF elements are used.

5 MULTIBODY EQUATIONS OF MOTION AND SOLUTION PROCEDURE

As previously mentioned, the numerical validation of the large deformation 3D FFR formulation is accomplished in this investigation by developing two computer models. The first is the FFR model, while the second is the ANCF model. The two models are based on two conceptually different formulations and employ different types of coordinates as discussed in the preceding section. The ANCF and FFR formulation also lead to different structures of the equations of motion. Nonetheless, the sparse matrix structure obtained using both formulations is effectively exploited in this study [4]. In this section, the constrained multibody system equations used in this investigation to study the large deformation robot dynamics are presented.

5.1 Equations of motion

The augmented form of the dynamic equations used in this investigation allows modelling rigid bodies as well as flexible bodies modelled using the ANCF or the FFR formulation. Joint constraints between different bodies are introduced using a set of non-linear algebraic equations, which are adjoined to the system differential equations using the technique of Lagrange multipliers. When explicit numerical integration methods are used, the constraint equations are satisfied at the position, velocity, and acceleration levels. The augmented form of the equations of motion that will be used in this paper can be written as [2]

$$\begin{bmatrix} \mathbf{M}_{rr} & \mathbf{M}_{rf} & 0 & \mathbf{C}_{\mathbf{q}_r}^T \\ \mathbf{M}_{fr} & \mathbf{M}_{ff} & 0 & \mathbf{C}_{\mathbf{q}_f}^T \\ 0 & 0 & \mathbf{M}_{aa} & \mathbf{C}_{\mathbf{q}_a}^T \\ \mathbf{C}_{\mathbf{q}_r} & \mathbf{C}_{\mathbf{q}_f} & \mathbf{C}_{\mathbf{q}_a} & 0 \end{bmatrix} \begin{bmatrix} \ddot{\mathbf{q}}_r \\ \ddot{\mathbf{q}}_f \\ \ddot{\mathbf{q}}_a \\ \boldsymbol{\lambda} \end{bmatrix} = \begin{bmatrix} \mathbf{Q}_r \\ \mathbf{Q}_f \\ \mathbf{Q}_a \\ \mathbf{Q}_c \end{bmatrix} \tag{20}$$

where subscripts r, f, and a refer, respectively, to reference, elastic, and absolute nodal coordinates, $\mathbf{M}_{rr}$, $\mathbf{M}_{rf}$, $\mathbf{M}_{fr}$, $\mathbf{M}_{ff}$ are the inertia sub-matrices that appear in the FFR formulation, $\mathbf{M}_{aa}$ is the ANCF constant symmetric

mass matrix, it is the identity matrix when Cholesky coordinates, $\mathbf{q}_a$, are used, $\mathbf{C_q}$ is the constraint Jacobian matrix, λ is the vector of Lagrange multipliers, $\mathbf{Q}_r$, $\mathbf{Q}_f$, and $\mathbf{Q}_a$ are the generalized forces associated with the reference, elastic, and absolute nodal coordinates, respectively, and $\mathbf{Q}_c$ is a quadratic velocity vector that results from the differentiation of the kinematic constraint equations twice with respect to time. The generalized coordinates, $\mathbf{q}_r$ and $\mathbf{q}_f$, are the FFR formulation coordinates used to describe the motion of rigid bodies as well as flexible bodies that experience large deformations in this investigation. The vector $\mathbf{q}_a$ is the same as the vector $\mathbf{e}$ if the ANCF Cholesky coordinates are not used [18]. The generalized forces used in equation (20) also include the elastic forces that result from the large deformation of the flexible bodies.

5.2 Computation algorithm

The second time derivative of the vectors of reference, elastic, and absolute nodal coordinates $\ddot{\mathbf{q}} = [\ddot{\mathbf{q}}_r^T \quad \ddot{\mathbf{q}}_f^T \quad \ddot{\mathbf{q}}_a^T]^T$ as well as the vector of Lagrange multipliers λ can be obtained by solving equation (20) using an LU algorithm. The vector of Lagrange multipliers can be used with the constraint Jacobian matrix to determine the generalized constraint forces of the joints in the system. Using the solution for the accelerations, one can define the state vector as $\mathbf{Y} = [\mathbf{q}^T \quad \dot{\mathbf{q}}^T]^T$, and the equations of motion obtained can be transformed into the following standard state-space form

$$\dot{\mathbf{Y}} = \begin{bmatrix} \dot{\mathbf{q}}^T & \ddot{\mathbf{q}}^T \end{bmatrix}^T = \mathbf{F}(\mathbf{Y}, t) \tag{21}$$

Given the initial conditions of the coordinates and velocities and a given integration time step Δt at time t_0, the preceding equation can be integrated forward in time to determine at time $t = t_0 + \Delta t$ the coordinates and velocities which can be used to reconstruct equation (20) using the coordinates and velocities at time t. The solution of equation (20) defines again the accelerations, which can be used to advance the integration.

The numerical solution procedure used in this investigation with explicit numerical integration methods is designed to ensure that the constraint equations are satisfied at the position, velocity, and acceleration levels. It is clear that equation (20) ensures that the constraint equations are satisfied at the acceleration level. In order to guarantee that the constraint equations $\mathbf{C}(\mathbf{q}, t) = 0$ are satisfied at the position and velocity levels, the independent accelerations are identified and integrated forward in time to determine the independent coordinates and velocities. Using the independent coordinates, an iterative Newton–Raphson algorithm can be used to solve the constraint equations $\mathbf{C}(\mathbf{q}, t) = 0$ for the dependent

coordinates. Having determined all the coordinates, the constraint equations at the velocity level $\mathbf{C_q}\dot{\mathbf{q}} + \mathbf{C}_t = 0$, where $\mathbf{C}_t$ is the partial derivative of the constraint equations with respect to time, can be solved using the generalized coordinate partitioning method for the dependent velocities. Determining the dependent velocities requires the solution of linear algebraic equations only.

6 AXIAL MODES AND IMPLICIT NUMERICAL INTEGRATION METHODS

In the case of stiff systems, explicit integration methods capture high-frequency contents in the solution by reducing the time step size. For this reason, these explicit methods can be very inefficient when stiff axial modes are included in the model to account for the geometric stiffness effects. For stiff systems that have widely separated eigenvalues, the use of implicit integration methods is recommended. Some implicit integration methods, which use iterative procedures such as Newton–Raphson algorithms and may include artificial damping, do not trace high-frequency components of the solution, and therefore, much larger time step size can be used, leading to a much more efficient solution procedure. Nonetheless, when the FFR formulation is used in the case of rotating beams, the effect of the stiff axial modes can be very significant particularly in the neighbourhood of critical speeds. In order to investigate the effect of filtering out high-frequency components of the solution, which is a characteristic of some implicit methods, the use of two implicit numerical integration methods is examined in the case of the large deformation analysis. These two implicit methods, which are briefly discussed in this section, are the Runge–Kutta and the HHT methods.

6.1 Implicit Runge–Kutta method: RADAU5

Runge–Kutta methods are representatives of the class of single-step numerical integration methods. Such methods make no use of the solution history. After determining the value $\mathbf{Y}_n$ as the numerical approximation of $\mathbf{Y}(t)$, the methods proceed to evaluate $\mathbf{Y}_{n+1}$ as an approximation of $\mathbf{Y}(t + \Delta t)$ according to the following formula

$$\mathbf{Y}_{n+1} = \mathbf{Y}_n + \Delta t \sum_{i=1}^{s} b_i \mathbf{k}_i$$

$$\mathbf{k}_i = \dot{\mathbf{Y}} \left(t_i + c_i \Delta t, \ \mathbf{Y}_i + \Delta t \sum_{j=1}^{s} a_{ij} \mathbf{k}_j \right), \ i = 1, 2, \ldots, s \tag{22}$$

Butcher tableau provides a representation of the *s-stage* Runge–Kutta methods. This table is given below

$$
\begin{array}{c|cccc}
c_1 & a_{11} & a_{12} & \cdots & a_{1s} \\
c_2 & a_{21} & a_{22} & \cdots & a_{2s} \\
\vdots & \vdots & \vdots & \ddots & \vdots \\
c_s & a_{s1} & a_{s1} & \cdots & a_{ss} \\
\hline
& b_1 & b_2 & \cdots & b_s
\end{array}
\Longleftrightarrow
\begin{array}{c|c}
\{c\} & \{a\} \\
\hline
& \{b\}^T
\end{array}
$$

For non-linear analysis, a fully implicit third stage and fifth-order accurate scheme, RADAU5 form, will be used as one step with constant step size Δt. In this case, the corresponding *Butcher tableau* is given by [**19**]

$$
\begin{array}{c|ccc}
\dfrac{(4-\sqrt{6})}{10} & \dfrac{(88-7\sqrt{6})}{360} & \dfrac{(296-169\sqrt{6})}{1800} & \dfrac{(-2+3\sqrt{6})}{255} \\[2ex]
\dfrac{(4+\sqrt{6})}{10} & \dfrac{(296+169\sqrt{6})}{1800} & \dfrac{(88+7\sqrt{6})}{360} & \dfrac{(-2-3\sqrt{6})}{255} \\[2ex]
1 & \dfrac{16-\sqrt{6}}{36} & \dfrac{(16+\sqrt{6})}{36} & \dfrac{1}{9} \\[2ex]
\hline
& \dfrac{(16-\sqrt{6})}{36} & \dfrac{(16+\sqrt{6})}{36} & \dfrac{1}{9}
\end{array}
$$

6.2 HHT integrator

The HHT integrator is based on the HHT method (known also as the α-method) [**20**, **21**]. This method is widely used in solving numerically second-order initial value problems in structural dynamics. The foundation of the HHT method is the Newmark method that was proposed by Newmark [**20**]. The Newmark method provides a solution for the structural dynamics equations of motion, which has the following standard form

$$
\mathbf{M}\ddot{\mathbf{q}} + \mathbf{D}\dot{\mathbf{q}} + \mathbf{K}\mathbf{q} = \mathbf{F}(t) \tag{23}
$$

where $\mathbf{q}$, $\dot{\mathbf{q}}$, and $\ddot{\mathbf{q}}$ are the vectors of generalized position coordinates, velocities, and accelerations, respectively, $\mathbf{M}$, $\mathbf{D}$, and $\mathbf{K}$ are the symmetric mass, damping, and stiffness matrices, respectively, and $\mathbf{F}$ is a time-dependent external force vector. Newmark method employs the following two equations that relate the position and the velocity vectors to the acceleration vector

$$
\mathbf{q}_{n+1} = \mathbf{q}_n + h\dot{\mathbf{q}}_n + \frac{h^2}{2}\left[(1-2\beta)\ddot{\mathbf{q}}_n + 2\beta\ddot{\mathbf{q}}_{n+1}\right]
$$
$$
\dot{\mathbf{q}}_{n+1} = \dot{\mathbf{q}}_n + h\left[(1-\gamma)\ddot{\mathbf{q}}_n + \gamma\ddot{\mathbf{q}}_{n+1}\right]
\tag{24}
$$

where $h = t_{n+1} - t_n$ is the step-size, and β and γ are two assumed parameters. By assuming that equation (23) is satisfied at any time, one can write the equations of motion at time t_{n+1} as follows

$$
\mathbf{M}\ddot{\mathbf{q}}_{n+1} + \mathbf{D}\dot{\mathbf{q}}_{n+1} + \mathbf{K}\mathbf{q}_{n+1} = \mathbf{F}(t_{n+1}) \tag{25}
$$

Substituting equation (24) into equation (25) and assuming that $\mathbf{q}_n$, $\dot{\mathbf{q}}_n$, and $\ddot{\mathbf{q}}_n$ are known, one obtains a set of equations that are functions of the acceleration vector $\ddot{\mathbf{q}}_{n+1}$. Therefore, these equations can be used to determine the vector of accelerations $\ddot{\mathbf{q}}_{n+1}$, which can be used in turn to determine $\mathbf{q}_{n+1}$ and $\dot{\mathbf{q}}_{n+1}$ using equation (24).

The HHT method is an improvement over the Newmark method in that it has the ability to eliminate undesirable high-frequency oscillations, while it remains stable and second-order convergent. The HHT method can be obtained by replacing equation (25) by

$$
\mathbf{M}\ddot{\mathbf{q}}_{n+1} + (1+\alpha)\mathbf{D}\dot{\mathbf{q}}_{n+1} - \alpha\mathbf{D}\dot{\mathbf{q}}_n + (1+\alpha)\mathbf{K}\mathbf{q}_{n+1}
$$
$$
- \alpha\mathbf{K}\mathbf{q}_n = \mathbf{F}(\tau_{n+1}) \tag{26}
$$

where α is an assumed parameter, and $\tau_{n+1} = t_n + (1+\alpha)h$. In order to obtain a stable solution using the implicit HHT method, the parameters α, γ, and β should be selected to satisfy the following relations

$$
-0.3 \leqslant \alpha \leqslant 0, \quad \gamma = \frac{1}{2} - \alpha, \quad \beta = \frac{(1-\alpha)^2}{4} \tag{27}
$$

The smaller the value of α, the more numerical damping is added to the system. The choice $\alpha = 0$ leads to the trapezoidal method, which has no numerical damping. Hussein *et al.* [**13**] demonstrated that the use of the HHT method can be very efficient as compared to the use of explicit methods when the ANCF fully parameterized finite elements that account for coupled deformation modes are considered.

7 EXPERIMENTAL VALIDATION

In this section, the test rig used to verify the modal frequencies and validate the large deformation FFR simulation results is described. A flexible single robot arm is used in this test rig.

7.1 Verification of modal frequencies

As shown in Fig. 3, the experimental test rig consists of a single-link lightweight structural steel robot arm. This test rig is used to obtain experimentally the eigen frequencies that are compared with numerical results obtained using the finite-element method. The PZT (lead zirconate titanate ($Pb[Zr_xTi_{1-x}]$)) sensor, with a model number ACX QP40W, is placed on the surface of the link. The output of the sensor is sent to the PC through a NI6024E D/A data acquisition card. Because of the difficulties associated with including the piezo sensor in the numerical model, it is important to find the minimum number of units

Fig. 3   Test rig

required for accurate description of the model. The
data of the robot link and the piezo sensor are pre-
sented in Table 1. The eigen frequency finite-element
results reported in this section are obtained using the
constant stiffness matrix $\mathbf{K}_{ff,L}$ previously defined in
this article. Table 2 shows a comparison between the
experimental and finite-element results. The finite-
element solution is obtained using different number
of elements in order to check the convergence of the
solution. It is clear from the results presented in Table 2
that using one element for modelling the flexible beam
does not lead to accurate convergent solution. For
the large deformation FFR model used in this inves-
tigation, the shapes of the first two modes associated
with frequencies 2.51 and 14.83 Hz are the most sig-
nificant. Based on the results presented in Table 2,
one can conclude that two finite elements are suffi-
cient for obtaining accurate eigen frequencies of the
beam. Figure 4 shows the mode shapes and their asso-
ciated frequencies. The results presented in this figure,
which show the numerical solution, indicate that the
ninth mode is an axial mode. The inclusion of the
shape of this mode in the large deformation FFR model
is necessary in order to capture important geometric
stiffness effects and obtain an accurate solution.

Table 1   Data used for the modal analysis experiment

	Beam	Piezo	Dimension
Length	0.6	0.101	M
Width	0.04	0.0381	M
Thickness	0.001	0.000 76	M
Young's modulus	200	63	GPa
Density	7800	7600	kg/m^3

Table 2   Modal frequencies (Hz)

Mode	1-Element	2-Elements	6-Elements	Experimental
1	2.283	2.2733	2.2722	2.51
2	22.493	14.36	14.243	14.83
3	91.239	48.569	39.944	41.25
4	890.11	90.853	78.634	
5	1454	140.96	90.81	
6	2326.5	570.93	131.1	
7		1352.8	196.15	
8		1910.5	302.44	
9		2164.4	415.4	
10		4725.8	566.33	
11		5330.8	567.64	
12		7561.2	767.79	

7.2   Verification of the large deformation FFR results

In order to verify the large deformation FFR results,
the experimental set-up shown in Fig. 5 is used. This
experiment consists of a single-link lightweight steel
manipulator driven by a DC brushless servo motor
with a built-in incremental encoder to indicate its
angular velocity. The hub is directly attached to the
motor shaft, and therefore, the link is directly driven
by the motor. A digital camera is fixed on the hub
(along the frame of the hub-body), which can cap-
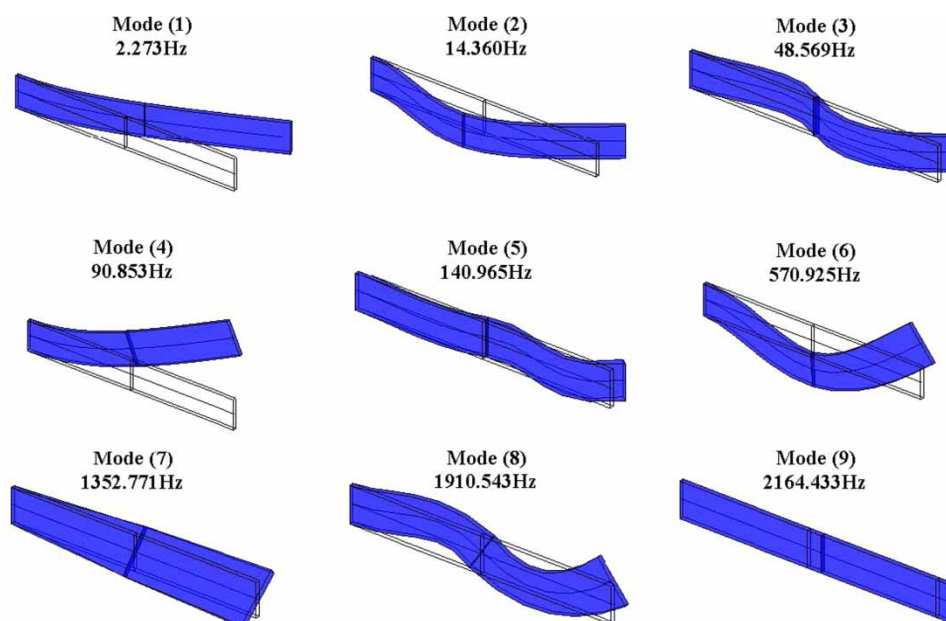ture the trace of an installed light-coloured tip mass;

Fig. 4   Mode shapes of the two-element beam

therefore, the tip point position can be recorded with respect to the frame of the camera. In Fig. 5, the laptop computer is the host PC, while the desktop computer is the target PC. In the real experiment, the real-time workshop within the XPC (registered tradmarks of the Mathworks, Inc.) target is used. The XPC is a host-target PC solution for prototyping, testing, and deploying real-time systems [**22**]. The XPC is used to avoid any delay in data acquisition. A significant delay is found if the traditional real-time workshop within the MATLAB is used. The test rig data are as follows: the hub mass is $m^1 = 0.515$ kg and mass moments of inertia are $\bar{I}_{xx}^1 = 9.9912 \times 10^{-4}$ kg m^2, $\bar{I}_{yy}^1 = 9.9686 \times 10^{-4}$ kg m^2, and $\bar{I}_{zz}^1 = 4.9394 \times 10^{-5}$ kg m^2. The torsional damping is identified as 0.015 N m s/rad and the effect of the torsional spring is not included in the model considered in this investigation.

7.3 Model construction

Figure 6 is a schematic representation of a two link system that is equivalent to the test rig described in this section. The first link represents the motor rotor and its attached hub, and the second link represents the rotating flexible arm. A revolute joint is used between the hub and the ground and a rigid joint is used between the hub and the flexible link. In the FFR model, two beam elements are used. In order to
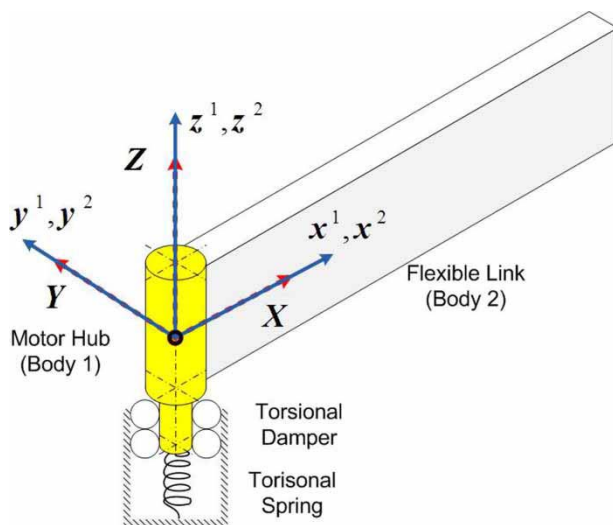
increase the efficiency of the experiment, the camera is used to record a movie for the tip point and the movie is processed to determine the tip point position. It is difficult to use the camera as a real-time measuring device because of two reasons: low shuttering speed of the camera and the unavailability of real-time video capture devices with the XPC target toolbox within MATLAB. In this experiment, a constant torque of $T_\theta = 0.1$ N m is fed forward from the host PC to the motor through the digital electronic device attached to the motor with closed-loop feedback to ensure the correct value of the torque. Since the critical speed is reached at time 3.5 s, the simulation and the experiment time is chosen to be 5 s. The recorded data of the tip point can be considered as the local transverse deflection of the tip point of the flexible arm.

8 COMPARISON BETWEEN SIMULATION AND EXPERIMENTAL RESULTS

The comparison between the results obtained using the non-linear FFR formulation and the ANCF-BC, ANCF-EL, and the experimental results are shown in Figs 7 and 8. In these figures, the transverse deformation of the tip point is shown as a function of time. The errors between the FFR model, ANCF-EL model, and the experimental results are shown in Fig. 9. In the FFR model, the first modal frequency that defines the critical speed of the flexible link if the effect of the geometric stiffening is not taken into account is 2.2733 Hz as shown in Table 2 for the two-beam element model. Because of the form of the applied torque, it is expected to reach the critical speed at time 3.5 s, as previously mentioned. In order to obtain correct results, the axial mode, which is the ninth mode as shown in Fig. 4, should be taken into account. Two approaches can be followed to select the necessary modal transformation of the model. The first approach is to select
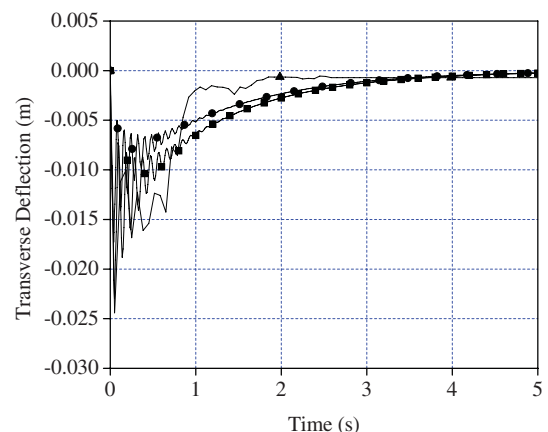

Fig. 6 Schematic diagram of the rotating flexible manipulator

Fig. 7 Transverse deflection (—■— FFR, —●— ANCF-BC, —▲— Experimental)
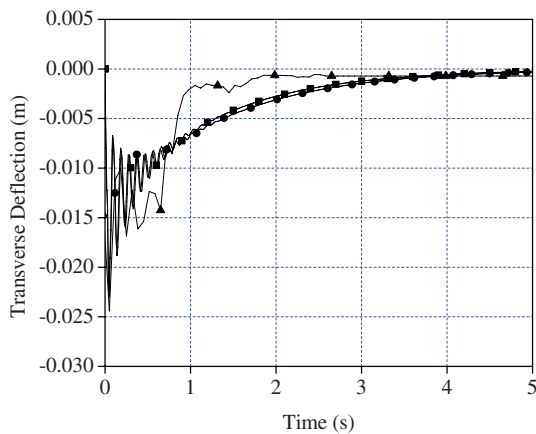
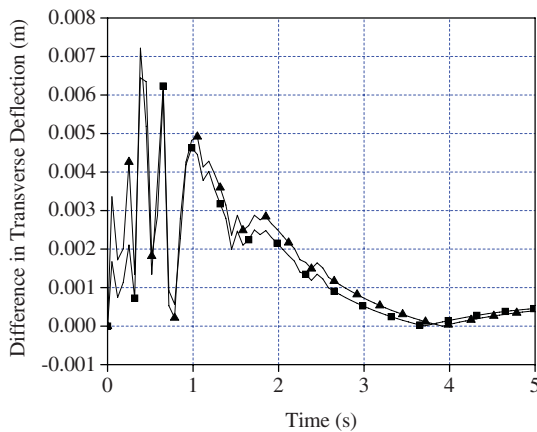**Fig. 8** Transverse deflection (——■—— FFR, ——●—— ANCF-EL, ——▲—— Experimental)

Fig. 9 Differences in transverse deflection from experimental results (——■—— FFR, ——▲—— ANCF-EL)
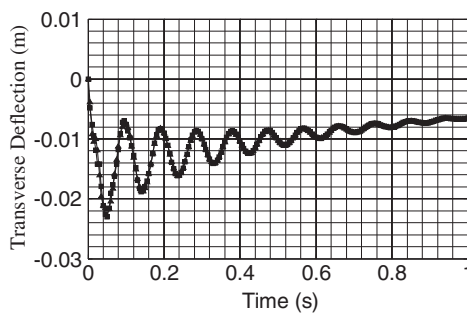

Fig. 10 Effect of modal reduction in the FFR model (——■—— 9 modes, ——▲—— 3 modes)

all the first nine modes by taking into account the first nine eigenvectors. The second approach is to select only the necessary modes, which are the first, the second, and the ninth modes. Figure 10 shows the transverse deflection of the rotating manipulator with and without modal reduction, a difference of 0.003 374 m is found at time 0.023 s. This difference disappears after 0.2 s.

8.1 Axial modes and implicit integration

The inclusion of high-frequency axial modes in the FFR dynamic models may be necessary in some applications in order to capture geometric stiffness that can have significant effects on the accuracy of the solution. Some implicit stiff numerical integration methods may fail to capture high-frequency geometric effects. Two implicit numerical integration methods are used in this study to obtain the numerical solutions of the models used. It is important to mention that the explicit fourth RK method failed from the start. The implicit integrator RADAU5 was successfully used to obtain the numerical results of the non-linear FFR model [1]. While numerical experimentation in this study demonstrated the robustness of RADAU5 to obtain the solution of the fast flexible link models, the computer time is much longer than the time required when the HHT integrator is used. The HHT integration method, however, failed to capture the geometric stiffness effect. It was found that, in the case of the undamped joint model, the solution does not converge when the critical speed is reached, as shown in Figs 11 and 12. For this reason, RADAU5 is used in the case of the FFR models.

8.2 ANCF-coupled deformation modes

Figure 13 shows the transverse deflection of the rotating manipulator models obtained using the ANCF finite-element model. Discrepancies between the ANCF-BC and ANCF-EL results can be noticed in the transient region, as shown in Fig. 14. It is clear that the integration of ANCF-coupled deformation modes included in the ANCF-BC solution is the source of the differences, and this difference becomes larger when the results are compared with experimental results. As it is known, for stiff and thin structure, fully parameterized ANCF finite elements can suffer
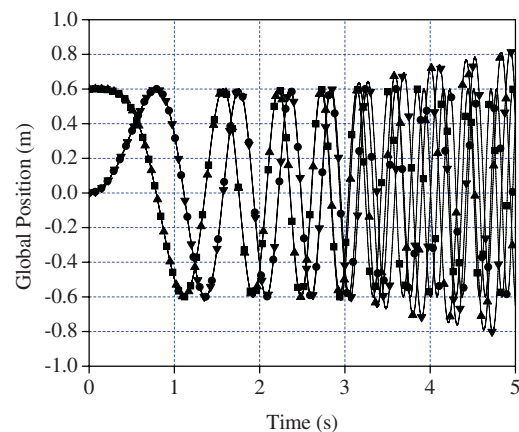

Fig. 11 Effect of integrator (FFR model – undamped joint) (——■—— X RADAU5, ——●—— Y RADAU5, ——▲—— X HHT, ——▼—— Y HHT)
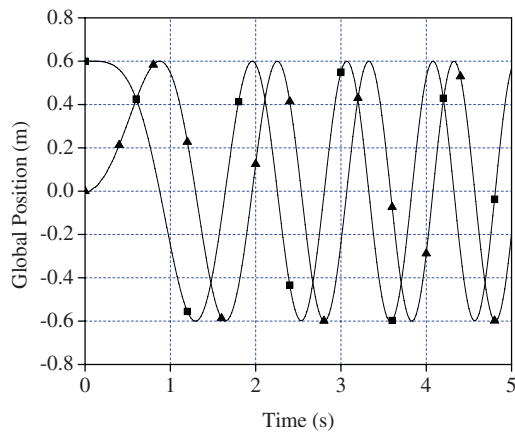
Fig. 12 Effect of damping (FFR model – damped joint) (——■—— X, ——▲—— Y)
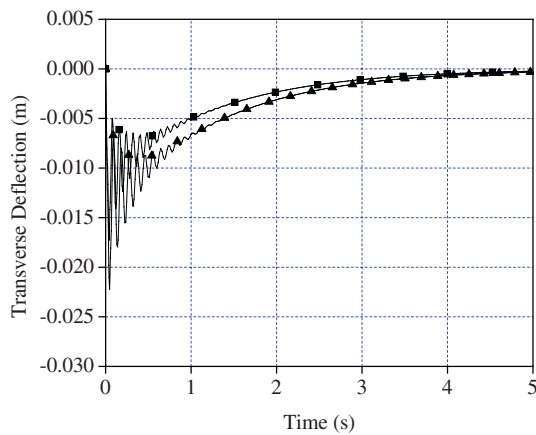

Fig. 13 Transverse deflection of ANC models of the rotating arm (——■—— ANCF-BC, ——▲—— ANCF-EL)
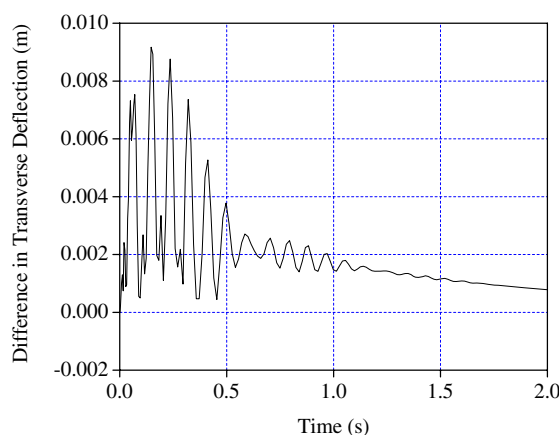

Fig. 14 Difference between ANCF-BC and ANCF-EL models

from locking problems. In the ANCF-EL, coupled deformation modes are eliminated, and therefore, the beam element model leads to a better agreement with the experimental results.

9 SUMMARY AND CONCLUSIONS

The FFR formulation has been widely used in the small deformation analysis of flexible multibody systems. This formulation allows for the use of modal representation, and therefore, a significant reduction of the model dimensionality can be achieved. The goal of this investigation is to demonstrate that the 3D FFR formulation can also be used in the large deformation analysis if such a deformation can be described using simple shapes. In this case, the inclusion of non-linear strain–displacement relationships is necessary in order to be able to capture the geometric stiffness effects which can be significant at certain speeds. Numerical and experimental validation was also another goal of this investigation. In order to numerically validate the non-linear FFR models, the solution of the rotating beam model considered in this investigation was obtained using the ANCF finite elements. The ANCF was used with two different elastic force formulations: the ANCF-BC and the ANCF-EL. It was shown that the solution of the ANCF-BC model, which includes high-frequency coupled deformation modes, does not agree with the experimental results. As it is known, in the case of thin and stiff structures, ANCF fully parameterized elements can suffer from locking which has an adverse effect on the accuracy of the solution. Good agreement, however, was observed between the FFR, ANCF-EL, and experimental results.

As discussed in this article, the inclusion of high-frequency axial modes in the FFR models may be necessary in order to capture the geometric stiffness that can have a significant effect on the solution. Nonetheless, some implicit integration methods filter out high frequencies and may fail to capture the effect of the high-frequency axial modes. Some of these integration methods use artificial damping in order to damp out high-frequency oscillations. Two different implicit integrators were used in this investigation to obtain the numerical solution of the finite-element models: the implicit RADAU5 and the HHT integrators. It was observed that the HHT integrator does not capture the effect of the axial mode in the non-linear FFR model. Nonetheless, the locking problems associated with the ANCF-BC models as the result of the coupled deformation modes can be avoided when the HHT method is used. The experimental and numerical validations of the non-linear FFR model presented in this study demonstrate that the FFR formulation can be effectively used in the large deformation analysis if the deformation assumes simple shapes.

ACKNOWLEDGEMENT

REFERENCES

1 **Nada, A. A.** *Flexible robotic manipulators: modeling, simulation and control with experimentation.* PhD Thesis, Mechanical Design and Production Engineering Department, Cairo University, Cairo, Egypt, 2007.

2 **Shabana, A. A.** *Dynamics of multibody systems,* 3rd edition, 2005 (Cambridge University Press, New York).

3 **Gerstmayr, J.** and **Schoberl, J.** A 3D finite element method for flexible multibody systems. *Multibody Syst. Dyn.,* 2006, **15**, 309–324.

4 **Orlandea, N. V.** From Newtonian dynamics to sparse tableaux formulation and multibody dynamics. *Proc. IMechE, Part K: J. Multi-body Dynamics,* 2008, **222**, 301–314. DOI: 10.1243/14644193JMBD153.

5 **Mikkola, A. M.** and **Matikainen, M. K.** Development of elastic forces for the large deformation plate element based on the absolute nodal coordinate formulation. *ASME J. Comput. Nonlinear Dyn.,* 2006, **1**(2), 103–108.

6 **Schwab, A. L.** and **Meijaard, J. P.** Comparison of three-dimensional flexible beam elements for dynamic analysis: finite element method and absolute nodal coordinate formulation. In Proceedings of the ASME International Design Engineering Technical Conferences and Computer and Information in Engineering Conference (DETC2005/MSNDC-85104), Long Beach, USA, 2005.

7 **Sopanen, J. T.** and **Mikkola, A. M.** Description of elastic forces in absolute nodal coordinate formulation. *Nonlinear Dyn.,* 2003, **34**(1–2), 53–74.

8 **Yoo, W. S., Lee, J. H., Park, S. J., Sohn, J. H., Pogorelov, D.,** and **Dimitrochenko, O.** Large deflection analysis of a thin plate: computer simulation and experiment. *Multibody Syst. Dyn.,* 2004, **11**(2), 185–208.

9 **Shampine, L.** and **Gordon, M.** *Computer solution of ODE: the initial value problem,* 1975 (W. H. Freeman, San Francisco).

10 **Garcia-Vallejo, D., Sugiyama, H.,** and **Shabana, A.** Finite element analysis of the geometric stiffening effect: a correction in the floating frame of reference formulation. *Proc. IMechE, Part K: J. Multi-body Dynamics,* 2005, **219**, 187–202. DOI: 10.1243/146441905X10041.

11 **Garcia-Vallejo, D., Sugiyama, H.,** and **Shabana, A.** Finite element analysis of the geometric stiffening effect: nonlinear elasticity. *Proc. IMechE, Part K: J. Multi-body Dynamics,* 2005, **219**, 203–211. DOI: 10.1243/146441905 X10050.

12 **Dmitrochenko, O. N., Hussein, B.,** and **Shabana, A. A.** Coupled deformation modes and their effect on the accuracy and efficiency of the large displacement finite element solutions: generalization. *ASME J. Comput. Nonlinear Dyn.,* 2009, **4**(2), 021002, 8 p.

13 **Hussein, B. A., Negrut, D.,** and **Shabana, A. A.** Implicit and explicit integration in the solution of the absolute nodal coordinate differential/algebraic equations. *Nonlinear Dyn.,* 2008, **54**(4), 283–296.

14 **Hussein, B. A., Sugiyama, H.,** and **Shabana, A. A.** Absolute nodal coordinate formulation coupled deformation modes: problem definition. *ASME J. Comput. Nonlinear Dyn.,* 2007, **2**(2), 146–154.

15 **Shabana, A. A.** and **Yakoub, R. Y.** Three dimensional absolute nodal coordinate formulation for beam elements: theory. *ASME J. Mech. Des.,* 2001, **123**(4), 606–613.

16 **Yakoub, Y. R.** and **Shabana, A. A.** Three dimensional absolute nodal coordinate formulation for beam elements: implementation and applications. *ASME J. Mech. Des.,* 2001, **123**(4), 614–621.

17 **García-Vallejo, D., Mayo, J., Escalona, J. L.,** and **Dominguez, J.** Efficient evaluation of the elastic forces and the Jacobian in the absolute nodal coordinate formulation. *Nonlinear Dyn.,* 2004, **35**(4), 313–329.

18 **Shabana, A. A.** *Computational continuum mechanics,* 2008 (Cambridge University Press, New York).

19 **Hairer, E.** and **Wanner, G.** Stiff differential equations solved by radau methods. In Proceedings of the Numerical Methods for Differential Equations, Coimbra, Portugal, 1999 (Elsevier North Holland, New York).

20 **Newmark, N. M.** A method of computation for structural dynamics. *J. Eng. Mech. Div., ASCE,* 1959, **85**, 67–94.

21 **Hilber, H. M., Hughes, T. J. R.,** and **Taylor, R. L.** Improved numerical dissipation for time integration algorithms in structural dynamics. *Earthq. Eng. Struct. Dyn.,* 1977, **5**, 283–292.

22 **Mosterman, P. J., Prabhu, S., Dowd, A., Glass, J., Erkkinen, T., Kluza, J.,** and **Shenoy, R.** *Embedded real-time control via MATLAB, simulink, and XPC target – book chapter,* 2005 (Birkhäuser Boston, Boston).

APPENDIX

Shape function matrix

The conventional beam element used in the FFR model has 12 degrees of freedom. The shape function of this element is given as

$$
\mathbf{S}^T = \begin{bmatrix}
1 - \xi & 0 & 0 \\
6(\xi - \xi^2)\eta & 1 - 3\xi^2 + 2\xi^3 & 0 \\
6(\xi - \xi^2)\zeta & 0 & 1 - 3\xi^2 + 2\xi^3 \\
0 & -(1-\xi)l\zeta & (1-\xi)l\eta \\
(1 - 4\xi + 3\xi^2)l\zeta & 0 & (-\xi + 2\xi^2 - \xi^3)l \\
(-1 + 4\xi - 3\xi^2)l\eta & (\xi - 2\xi^2 + \xi^3)l & 0 \\
\xi & 0 & 0 \\
6(-\xi + \xi^2)\eta & 3\xi^2 - 2\xi^3 & 0 \\
6(-\xi + \xi^2)\zeta & 0 & 3\xi^2 - 2\xi^3 \\
0 & -l\xi\zeta & l\xi\eta \\
(-2\xi + 3\xi^2)l\zeta & 0 & (\xi^2 - \xi^3)l \\
(2\xi - 3\xi^2)l\eta & (-\xi^2 + \xi^3)l & 0
\end{bmatrix}
$$

In this equation, $\xi = x/l, \eta = y/l, \zeta = z/l$, and l is the length of the element.